

# Synergistic Integration of Carbon Nanotubes and Vertically Aligned Graphene Enables Silicon as Stable and High-Rate Anodes in Lithium-Ion Batteries

Fenghua Yu, Yongbiao Mu, Meisheng Han,\* Hengyuan Hu, Zhiyu Zou, Kunxiong Zheng, Yuankai Huang, Wenjia Li, Lei Wei,\* Lin Zeng,\* and Tianshou Zhao\*

As the demand for high-energy-density lithium-ion batteries grows, research increasingly focuses on high-capacity anode materials to substitute low-capacity graphite. Silicon is a promising, high-theoretical-capacity ( $4200 \text{ mAh g}^{-1}$ ) anode material. However, suffering from severe volumetric expansion ( $\approx 400\%$ ) and poor conductivity ( $\approx 10^{-5} \text{ S cm}^{-1}$ ), the silicon anode shows unsatisfactory cycling stability and rate performance. Here, a 3D interconnected conductive and porous carbon network is constructed by self-assembling carbon nanotubes onto silicon nanoparticles encapsulated in vertically aligned graphene through the spray drying method. The carbon network provides efficient space, accommodating volumetric expansion of Si. Vertical

graphene provides directional ion transportation and carbon nanotubes accelerate the electron transfer due to their high conductivity. The collaboration constructs a 3D robust conductive network to boost charge transport throughout the electrode. With these structural advantages, the electrodes deliver high capacities of  $904 \text{ mAh g}^{-1}$  at  $5 \text{ Ag}^{-1}$  with high capacity retention of 78.0% after 1000 cycles and  $418 \text{ mAh g}^{-1}$  at  $20 \text{ Ag}^{-1}$ , while exhibiting only a 2.6% thickness change in the cross-sectional direction after 100 cycles at  $0.5 \text{ Ag}^{-1}$ . Furthermore, the lithium storage mechanism of the silicon–carbon anode is elucidated through cyclic voltammetry and ex situ X-ray diffraction.

## 1. Introduction

As high-energy-density and high-operating-voltage energy storage devices, lithium-ion batteries (LIBs) are widely utilized in portable electronics and electric vehicles.<sup>[1,2]</sup> However, as a commercially dominant anode, graphite's relatively low theoretical capacity of  $372 \text{ mAh g}^{-1}$  imposes a significant limitation on the improvement of energy density of batteries,<sup>[3]</sup> thereby restricting the usage time after a single charging of various electronic devices such as smartphones, electric vehicles, and drones.<sup>[4,5]</sup> To address this challenge and enhance the energy density of batteries, researchers have primarily focused on increasing the specific capacity of anode materials. Among the numerous anode materials under

investigation, silicon has emerged as one of the most promising candidates due to its exceptionally high theoretical capacity ( $4200 \text{ mAh g}^{-1}$ ) and favorable electrochemical properties.<sup>[6]</sup> This extraordinary capacity opens the possibility of significantly boosting the energy density of LIBs. In addition to its high capacity, silicon also features a relatively safe lithiation potential ( $\approx 0.2 \text{ V}$ ), which lies above the voltage threshold for lithium dendrite formation, thereby suppressing dendrite growth during rapid charge–discharge processes and improving overall battery safety.<sup>[7]</sup> Despite these advantages, several challenges hinder the practical application of silicon as an anode material. First, silicon possesses poor intrinsic electronic conductivity ( $\approx 10^{-5} \text{ S cm}^{-1}$ ),<sup>[8]</sup> limiting the efficient transport of electrons during charge and discharge cycles. More critically, silicon undergoes drastic volume expansion, up to  $\approx 400\%$  during lithiation.<sup>[9,10]</sup> These repeated expansions and contractions introduce severe mechanical stress, often leading to pulverization and detachment of the active material from the current collector.<sup>[11]</sup> Consequently, the electrode structure degrades, and the battery capacity rapidly declines.<sup>[12]</sup> Furthermore, the continuous volume fluctuations disrupt the solid electrolyte interphase (SEI) layer, which is vital for stabilizing the electrode–electrolyte interfaces. The repeated damage to the SEI consumes excessive amounts of electrolyte and leads to poor cycling stability and sub-optimal rate performance.<sup>[13,14]</sup> Although pure silicon anodes offer an exceptionally high theoretical capacity, their practical deployment is limited by inherent drawbacks such as low conductivity, substantial volume expansion, and unstable electrode–electrolyte interfaces.<sup>[15]</sup> Addressing these issues is crucial for the successful integration of silicon into commercial LIB systems.

F. Yu, Y. Mu, M. Han, H. Hu, Z. Zou, K. Zheng, Y. Huang, W. Li, L. Wei, L. Zeng, T. Zhao

Shenzhen Key Laboratory of Advanced Energy Storage

Department of Mechanical and Energy Engineering

Southern University of Science and Technology

Shenzhen 518055, China

E-mail: hanms@sustech.edu.cn

weil@sustech.edu.cn

zengl3@sustech.edu.cn

zhaots@sustech.edu.cn

F. Yu, Y. Mu, M. Han, H. Hu, Z. Zou, K. Zheng, Y. Huang, W. Li, L. Wei, L. Zeng, T. Zhao

SUSTech Energy Institute for Carbon Neutrality

Southern University of Science and Technology

Shenzhen 518055, China



Supporting information for this article is available on the WWW under <https://doi.org/10.1002/batt.202500648>

To address the key challenges of low electrical conductivity, substantial volume expansion, and interfacial instability in silicon-based anodes for LIBs, a widely adopted strategy involves the nanostructuring of silicon followed by compositing with carbon materials.<sup>[16]</sup> Commonly employed carbon materials include graphene, carbon nanotubes (CNTs),<sup>[17,18]</sup> and amorphous carbon.<sup>[19]</sup> In recent years, substantial progress has been achieved by optimizing composite configurations and structural designs to enhance the conductivity of silicon–carbon (Si–C) anodes and to mitigate the adverse effects of silicon’s volume changes on electrode performance. Han et al. demonstrated that the growth of vertically aligned graphene (VG) on the surface of silicon-based materials can significantly improve their cycling stability and rate capability,<sup>[20]</sup> owing to the porous and flexible characteristics of VG. In their study, chemical vapor deposition was employed to deposit carbon atoms onto silicon surfaces, where nucleation occurs. Through the fusion of oppositely oriented carbon layers, radially grown graphene nanosheets are formed, resulting in a VG architecture relative to the substrate. This structure allows the graphene layers to slide during the charge–discharge cycles, thereby accommodating the volume changes of the silicon and relieving internal stress, which enhances cycling stability. Furthermore, the VG layers create continuous electron pathways. The interconnected network significantly improves the electrical conductivity via multipoint contact instead of single-point contact, thus enhancing the rate performance of the Si anode. Core-shell carbon coating is another commonly explored approach for addressing the volume expansion issues of silicon. Wu et al. proposed a dual-layer coated silicon-based composite anode.<sup>[21]</sup> The Si–C composite, prepared through high-energy ball milling with phenolic resin as the carbon source, represents a hard carbon shell on the surface of the silicon particles. This shell acts as a barrier, reducing direct contact between the silicon and the electrolyte, thereby suppressing unwanted side reactions and minimizing the consumption of lithium salts and active material. Moreover, the carbon shell with superior electronic conductivity compared to silicon, facilitates improved electron transport when it encapsulates the poorly conductive silicon, effectively enhancing the overall conductivity of the Si–C anode. This core-shell Si–C composite exhibits high initial Coulombic efficiency, excellent rate performance, and stable cycling behavior. Besides, the incorporation of CNTs has also been regarded as a key strategy to maintain both the electrical conductivity and cycling stability of silicon anodes. One approach proposed by He et al. involves constructing a networked CNT framework:  $\text{SiO}_x@\text{C}$  is assembled with CNTs by electric field orientation.<sup>[22]</sup> While this strategy offers improvements in performance, challenges remain. The inherent "piercing effect" of CNTs and the formation of excessively thick SEI are concerns in CNT-based Si–C anodes.<sup>[23]</sup> These can cause mechanical damage to the SEI layer, leading to electrical disconnection, thus decreasing Coulombic efficiency and cycling stability. Various Si–C composite approaches using carbon materials have been extensively explored. However, each comes with limitations. Vertically aligned graphene encapsulating nanoSi often obtains low tapping density and electrical conductivity of powders due to their loose structure, decreasing the volumetric capacity and rate performances. Core-shell

coatings restrict the available space for silicon’s expansion, leading to excessive internal stress, carbon shell fracture, and deterioration of cycling performance. Meanwhile, simple CNT-based composites may have fewer ion-conductive pathways, which hinder efficient ionic transportation.

This study is devoted to developing a stable silicon–carbon composite anode by combining vertically grown graphene-coated silicon nanoparticles with CNTs, enhancing the conductivity of both lithium-ion and electrons. Investigating the lithium storage mechanism through various characterization techniques is also involved. The research is primarily carried out based on the following approaches and methodology: vertically aligned graphene silicon nanoparticles are used as the core material, and encapsulated by CNTs shell via a spray-drying process, forming a structure in which the CNTs and graphene are nearly perpendicular in spatial orientation. This architecture provides enhanced stability with the SEI and sufficient space to accommodate silicon’s volume changes. The resulting material is subjected to comprehensive morphological, structural, and compositional analyses. Furthermore, the electrochemical performance of the composite anode is systematically evaluated, including electrochemical impedance spectroscopy (EIS), cyclic voltammetry (CV), cycling stability, and rate capability tests. Structural characterizations are performed on electrodes cycled under various voltage cutoffs, and electrodes after different numbers of cycles are compared in terms of morphology, composition, and microstructure. Through these analyses, the study aims to present how the integration of CNTs and VG structures influences the lithium storage performance of the Si anode. Ultimately, the goal is to reveal the stable and fast lithium storage mechanism of this silicon–carbon composite anode, offering new insights into the design of high-performance silicon-based materials for next-generation LIBs.

## 2. Results and Discussion

Figure 1a shows the synthesis strategy for vertically graphene-encapsulated silicon nanoparticles (SiVG) with CNTs covered, and the corresponding obtained sample is labeled as SiVG<sub>2T</sub> (its detailed preparation process is described in Supporting Information). The spray-drying process in the preparation strategy provides a self-assembled, 3D, stable carbon network that consists of VG and CNTs. With the carbon network, the internal stress of the anode due to the volumetric variation of Si during the charging/discharging process can be reduced (Figure 1b). The scanning electron microscopy (SEM) images of SiVG are shown in Figure 1c–e. On the pristine SiVG, distinct, uniform, and porous vertical graphene encapsulation on the Si nanoparticles can be observed. Regarding the encapsulation configuration of porous, flexible VG, each individual provides sufficient strain accommodation space. However, when vertically aligned graphene silicon nanoparticles are stacked, the graphene layers may intrude into the reserved spaces of adjacent particles, potentially reducing the available strain space for silicon volumetric expansion. After spray-drying and self-assembling with CNTs, the CNTs are able to uniformly coat the SiVG. When the mass ratio of SiVG to CNTs is

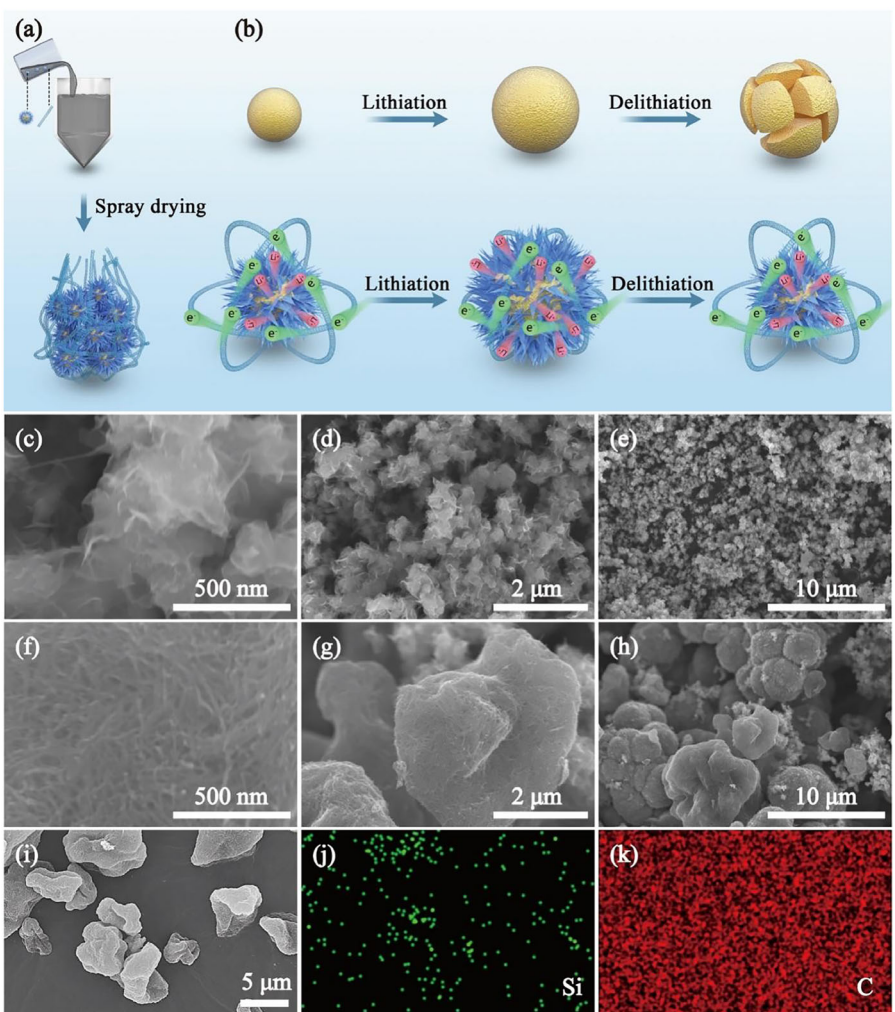


**Figure 1.** Schematic diagrams of a) preparation process and b) structural stability during cycling of  $\text{SiVG}_2\text{T}$ , along with SEM images of c–e)  $\text{SiVG}$ , f–h)  $\text{SiVG}_2\text{T}$ . i) EDS images of  $\text{SiVG}_2\text{T}$ , of j) Si and k) C.

2:1, the composite material is denoted as  $\text{SiVG}_2\text{T}$ , with the highly uniform coverage of CNTs on the  $\text{SiVG}$  particles (Figure 1f–h). A dense multilayer CNT coating is formed on the top of the VG, making it nearly impossible to distinguish the contour of the  $\text{SiVG}$  nanoparticles under SEM, appearing instead as CNT-coated microspherical particles. This encapsulation not only constructs a three-dimensional electronic transport network, providing excellent electrical conductivity, but also maintains favorable ion transport pathways. Furthermore, the particle size is enlarged from nanoscale (200–300 nm) to microscale (3–8  $\mu\text{m}$ ), which may enhance the electronic conductivity with a more organized electrical network. To verify the uniformity of the elemental distribution and morphology of the  $\text{SiVG}_2\text{T}$ , energy-dispersive spectroscopy (EDS) was conducted on the samples. In the EDS mapping analysis, regions with comparable material thickness were selected, and thus, the relative point density in the EDS maps can be used as a qualitative indicator of the relative elemental content.  $\text{SiVG}$  exhibits a relatively higher silicon content, confirming the presence and high content of silicon, which is consistent with the initial carbon-to-silicon ratio of the raw materials.

The silicon and carbon distribution within the  $\text{SiVG}$  aligns, to some extent, with the morphology observed in the SEM images, demonstrating an overall uniform distribution without noticeable agglomeration of individual components, as illustrated in (Figure S1, Supporting Information). In contrast,  $\text{SiVG}_2\text{T}$  contains a larger amount of CNTs, which leads to an increased carbon content and a corresponding decrease in the silicon mass fraction. The weaker silicon signal in the EDS maps of  $\text{SiVG}_2\text{T}$  validates the designed compositional ratio (Figure 1i–k). The EDS results confirm that the elements in  $\text{SiVG}$  and  $\text{SiVG}_2\text{T}$  are uniformly distributed, potentially providing electrochemical uniformity during cycling.

Compared with the perspective provided by SEM, transmission electron microscopy (TEM) allows for the observation of finer microstructural details of the composite material. As shown in Figure 2a–c, the silicon nanoparticles have an average size of  $\approx 150$  nm, while the VG with a height of around 40 nm is uniformly distributed and present in sufficient quantity on the silicon surface to support the subsequent coating of CNTs. At the bottom of VGs, the number of graphene layers is about 10. Furthermore, at the top edge of VGs, the number of graphene layers is one. The

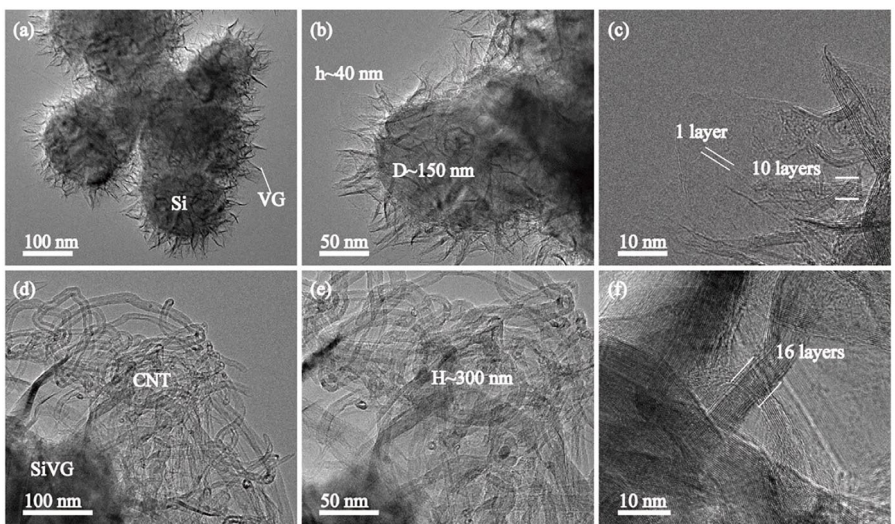
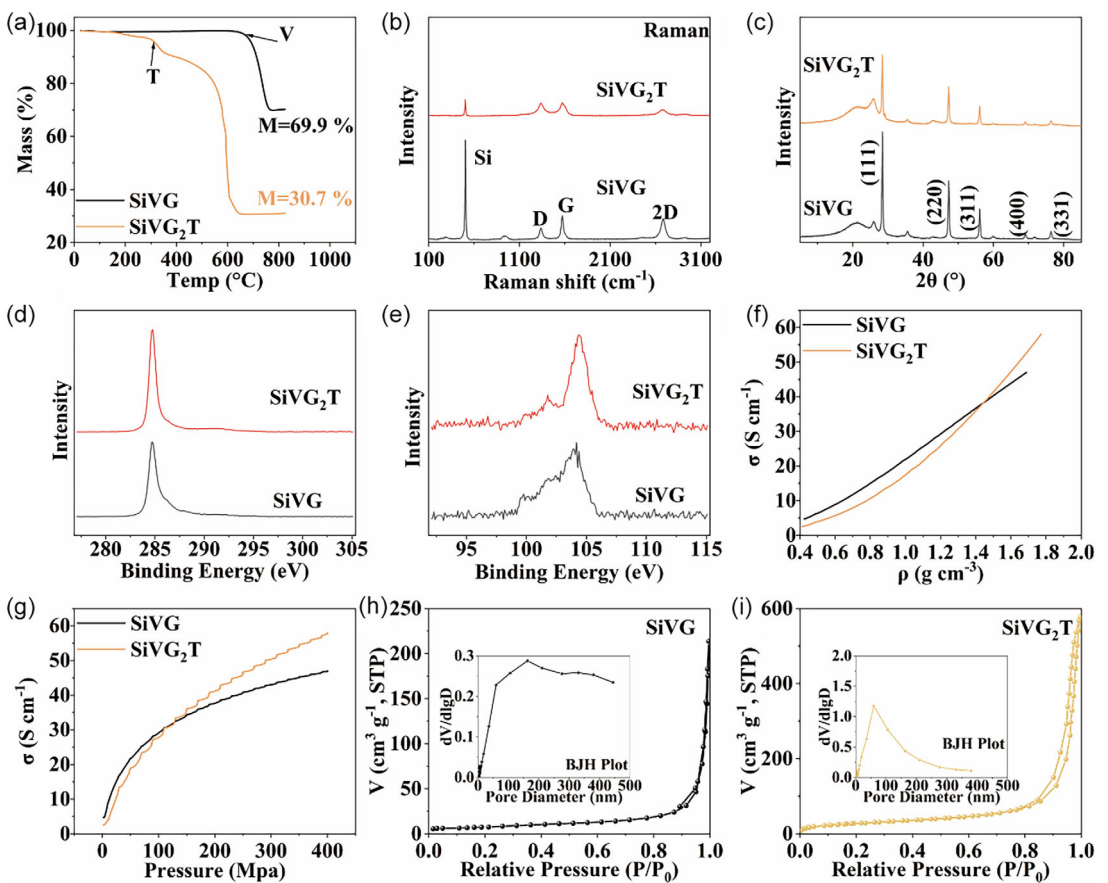


Figure 2. TEM images of a–c) SiVG and d–f) SiVG<sub>2</sub>T.

presence of CNTs in SiVG<sub>2</sub>T is more evident in Figure 2d–f, where multiwall CNTs are observed coating the surfaces of SiVG particles, which is consistent with the SEM results. The thickness of the CNT coating is around 300 nm and consists of roughly 16 carbon layers. This hierarchical structure not only provides excellent electronic conductivity but also shortens the ion transport pathways, thereby enhancing electrochemical performance.

According to the thermogravimetric analysis (TGA) results, when heating is conducted under an air atmosphere, carbon is oxidized to form carbon dioxide, leading to a decrease in mass. Graphene exhibits a relatively high thermal decomposition temperature. Experimental results show that the final stage of thermal decomposition of the SiVG occurs at a higher temperature. As indicated by point V (Figure 3a), the decomposition temperature of SiVG is ≈650 °C. At point T, the decomposition of CNTs begins, with a decomposition temperature of around 300 °C. The final mass value is taken as the lowest point in the experiment to minimize interference from silicon oxidation. Based on the residual mass, the silicon content of SiVG is ≈69.9 wt%, while that of SiVG<sub>2</sub>T is 30.7 wt%. As estimated from TGA results, the ratio of SiVG is around 43.9% in SiVG<sub>2</sub>T. To investigate the composition and chemical state of the two silicon–carbon composites, Raman spectroscopy (Figure 3b) was performed on the fully prepared materials. Due to its higher silicon content, SiVG exhibits the strongest silicon characteristic peak at 503 cm<sup>-1</sup>. In SiVG<sub>2</sub>T, the intensity of the 2D peak, which is a characteristic peak of graphene, also correlates with the content of the SiVG, further indicating that the preparation method has little influence on the structure of graphene or the raw material ratios. The D and G peaks in the spectra are at 1337 and 1574 cm<sup>-1</sup>, respectively.<sup>[24]</sup> The ratio of I<sub>D</sub>/I<sub>G</sub> represents the disorder characteristics of carbon materials. As a result, a higher I<sub>D</sub>/I<sub>G</sub> ratio in SiVG indicates that it has more graphitic carbon than SiVG<sub>2</sub>T. X-ray diffraction (XRD) patterns (Figure 3c) further confirm the presence of silicon, with characteristic peaks observed at 28.5°, 47.3°, 56.1°, 69.1°, and 76.4°, corresponding to the (111), (220), (311), (400), and (331)

crystal planes of silicon, respectively, referring to PDF#27–1402. These results demonstrate that the crystalline structure of silicon remains intact and is not affected by the composite formation or carbon deposition processes.<sup>[25]</sup> Moreover, the relative intensities of these peaks reflect the silicon content in each sample, which aligns with the designed ratios. SiVG has the higher silicon content, as evidenced by a higher (111) peak intensity, whereas SiVG<sub>2</sub>T shows a lower intensity, confirming that the addition of CNTs leads to a decrease in the silicon mass fraction. After the combination of SiVG and CNTs, X-ray photoelectron spectroscopy (XPS) reveals a certain increase in carbon content, while the properties and chemical states of silicon remain essentially unaffected, as illustrated in Figure 3d,e, and (Figure S2, Supporting Information). The lithium-storage capability of silicon is thus preserved, maintaining its high-capacity potential. For the uncomressed powder form of the silicon–carbon material, SiVG, due to the absence of CNTs integration, may form a denser and more conductive structure through the coupling of vertical graphene layers, as shown in (Figure S3a, Supporting Information). However, after the composite is formed with CNTs, the electrical conductivity of the material is slightly lower than that of the pristine SiVG. This reduction is attributed to the CNTs coating, which provides a more stable and larger strain accommodation space to alleviate the adverse effects of silicon volume expansion on the anode. In the tap-density and electrical conductivity measurements, at the same compact density, the sample with CNTs exhibits higher electrical conductivity after the increase in compact density (Figure 3f). Figure 3g further indicates that the addition of CNTs does not necessarily enhance the performance of SiVG<sub>2</sub>T. However, beyond a certain CNT loading and under a specific applied pressure of 110 MPa for these materials, the electrical conductivity of the SiVG<sub>2</sub>T surpasses that of the original SiVG. The resistivity results are consistent with the electrical conductivity trends, as shown in (Figure S3b, Supporting Information). The actual tested electrodes need to be rolled, and the electrode compaction density for commercial microsized material is usually between 1.6 and 2.0 g cm<sup>-3</sup>.



**Figure 3.** a) TGA plots, b) Raman spectra, c) XRD patterns, XPS spectra of d) C and e) Si, f) density-conductivity curves, and g) pressure-conductivity curves of SiVG and SiVG<sub>2</sub>T. h,i) BET plots of (h) SiVG and (i) SiVG<sub>2</sub>T.

It is obvious that SiVG<sub>2</sub>T, which has been highly compacted, has higher conductivity, benefiting the formation of a more developed conductive network at the electrode level to facilitate electron transfer. Nitrogen adsorption–desorption analysis was conducted on the samples. The silicon–carbon materials in this study did not exhibit any distinct adsorption–desorption plateaus on the isotherms, indicating that the pore structures of these materials are irregular. The specific surface area measured by the Brunauer–Emmett–Teller (BET) method of SiVG and SiVG<sub>2</sub>T are 27.61 (Figure 3h) and 102.88 ( $\text{m}^2 \text{ g}^{-1}$ ) respectively. A higher specific surface area facilitates more thorough contact between the electrolyte and active material, thus accelerating lithium ion transport and improving rate performance. Furthermore, the BJH pore size distribution results show that the pore size of SiVG is mainly concentrated above 70 nm (Figure 3h). Compared with SiVG<sub>2</sub>T, the porosity of pristine SiVG likely originates from the stacking between graphene layers. In contrast, SiVG<sub>2</sub>T demonstrates more effective encapsulation by CNTs, resulting in a more controlled pore size distribution centered around 100 nm (Figure 3i).

The initial discharge capacity is closely related to the silicon content; generally, a higher silicon mass fraction corresponds to a higher initial charge capacity. Microsized materials (SiVG<sub>2</sub>T, Figure 1h) have a higher tap density than nanosized materials (SiVG, Figure 1e), resulting in a higher electrode compaction

density. Under the same mass loading, a higher compaction density results in a lower electrode thickness. To demonstrate the synergistic effect of vertical graphene and CNTs on stability and rate performances, the same areal capacity and electrode thickness of SiVG and SiVG<sub>2</sub>T should be obtained, resulting in different mass loadings of active materials (specific values shown in Supporting Information). In the initial charge/discharge curves, the discharge plateau remains largely unaffected by the presence of CNTs. The initial discharge capacities of SiVG and SiVG<sub>2</sub>T are 2397 and 1630  $\text{mAh g}^{-1}$ , respectively, while their initial charge capacities are 1610 and 1122  $\text{mAh g}^{-1}$  at 0.1  $\text{A g}^{-1}$ , as shown in Figure 4a. This yields initial Coulombic efficiencies of 67% and 69%, respectively. The relatively low initial Coulombic efficiency of the silicon–carbon composites is likely due to the formation of an SEI layer during the first cycle, ascribed to the decomposition of the electrolyte. As shown in Figure 4b, the initial reversible specific capacities of SiVG and SiVG<sub>2</sub>T are 1556 and 1056  $\text{mAh g}^{-1}$ , respectively. The value of areal capacities is calculated as 1.415 and 0.973  $\text{mAh cm}^{-2}$ , respectively. After 100 cycles at a current density of 0.5  $\text{A g}^{-1}$ , the discharge capacities of SiVG and SiVG<sub>2</sub>T are 1260 and 914  $\text{mAh g}^{-1}$ , respectively, with corresponding capacity retentions of 81% and 87%. Under this current density, SiVG shows relatively lower cycling stability. The addition of CNTs contributes to improved capacity retention to some extent. In the

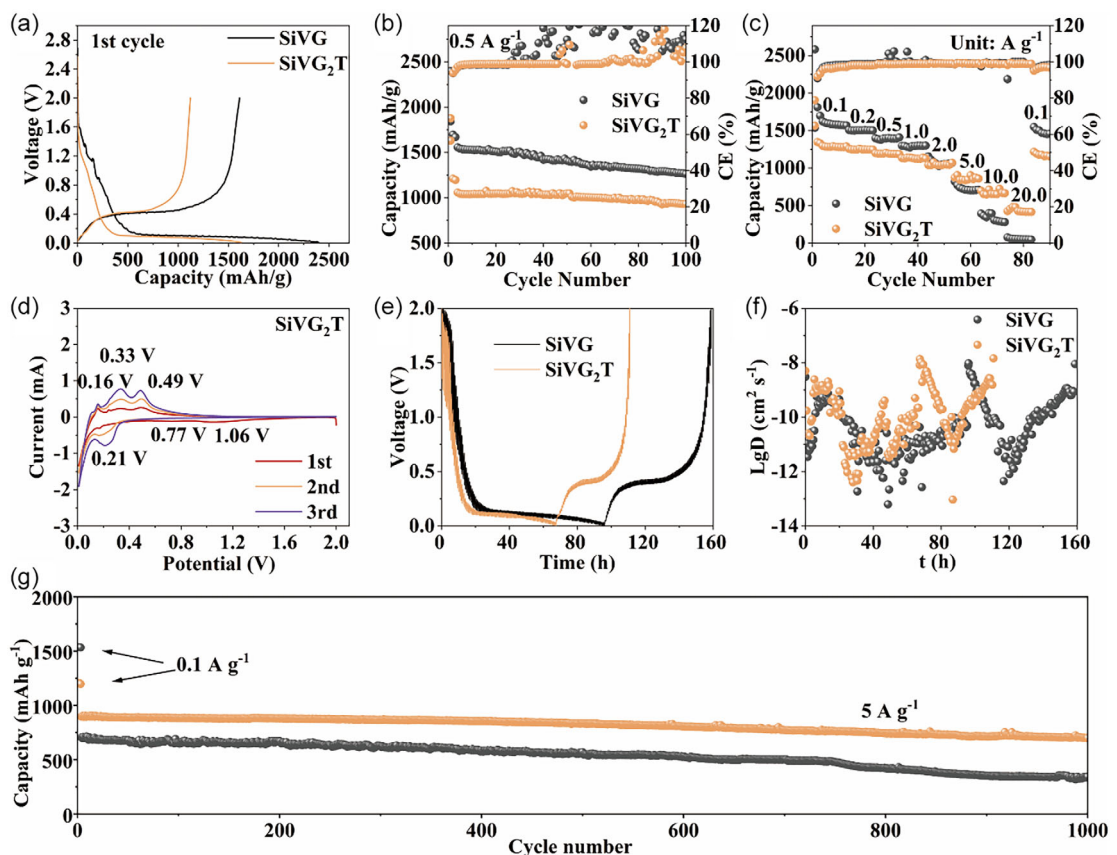


**Figure 4.** Electrochemical performance. a) Charge/discharge curves at the first cycle at  $0.1 \text{ A g}^{-1}$ , b) cycling performance at current density of  $0.5 \text{ A g}^{-1}$ , and c) rate capabilities of SiVG and SiVG<sub>2</sub>T. d) CV test of SiVG<sub>2</sub>T at  $0.1 \text{ mV s}^{-1}$ , e) GITT curves of SiVG and SiVG<sub>2</sub>T, f) corresponding diffusion coefficient, and g) cycling curves of SiVG and SiVG<sub>2</sub>T.

rate performance tests, the SiVG<sub>2</sub>T exhibits higher capacities than SiVG at current densities of  $2 \text{ A g}^{-1}$  and above. At  $5 \text{ A g}^{-1}$ , the capacities of SiVG and SiVG<sub>2</sub>T were 704 and  $905.9 \text{ mAh g}^{-1}$ , respectively. To investigate the relationship between the CNT-to-SiVG mass ratio and electrochemical performance, the materials composing of SiVG and CNT with the mass ratio of 5:1 and 1:1 are synthesized and remarked as SiVG<sub>5</sub>C and SiVG<sub>1</sub>C, respectively, and the corresponding electrochemical performances are shown in (Figure S4a–c, Supporting Information). Combined with the results in Figure 4, the ICE, stability at high current density, specific capacity, and rate capability of the composites with different mass ratios of CNT are summarized in (Table S1, Supporting Information). Obviously, as the CNT content increases, the ICE and cycling stability are gradually enhanced but the corresponding specific capacity is decreased. This is because the electrodes' volume expansion and lithium storage capacity are mainly from the Si contribution. More CNTs coating means less Si content, which would result in a lower capacity and an enhanced cycling stability, and decreases the electrolyte side reactions to enhance the ICE. The rate capability is first increased and then decreased with the increase of CNT content. This is because electron conduction is mainly enhanced by CNTs and the ionic conductivity is mainly determined by the VG. Excess VG for SiVG and excess CNTs for SiVG<sub>5</sub>C would be unfavorable for electron transfer and ion

transport, respectively, thus the cooperation of VG and CNTs is an effective strategy to improve the rate capability at an appropriate mass ratio, in this work, namely 2:1. Clearly, the rate capability of SiVG<sub>2</sub>T is the best among these anodes, reaching  $418 \text{ mAh g}^{-1}$  at  $20 \text{ A g}^{-1}$ . The rate performance is also compared to similar works. Due to the various current densities, the specific capacity at  $5 \text{ A g}^{-1}$  in this work is selected to compare with those below  $5 \text{ A g}^{-1}$ , in which the value of some works is calculated instead of being directly obtained (Figure S4d, Supporting Information). This improvement can be attributed to the enhanced conductivity and high structural stability of the conductive network of electrodes provided by the CNTs, which partially mitigates the poor intrinsic conductivity of silicon and thus improves the rate performance of the silicon-based anode (Figure 4c, (Figure S5, Supporting Information)). In the CV tests, two reduction peaks disappear after the first cycle, indicating that the SEI layer is formed at  $\approx 0.77$  and  $1.1 \text{ V}$ . As shown in Figure 4d, the current required for SEI formation is significantly lower in SiVG<sub>2</sub>T compared to SiVG, suggesting reduced electrolyte consumption and, consequently, a higher Coulombic efficiency for SiVG<sub>2</sub>T. The oxidation peaks at  $0.33$  and  $0.49 \text{ V}$  correspond to the delithiation (dealloying) of silicon.<sup>[26]</sup> In SiVG<sub>2</sub>T, an additional oxidation peak at  $0.16 \text{ V}$  is generally attributed to the delithiation of graphitic carbon, likely due to the graphitized components within the CNTs.<sup>[27]</sup> Since SiVG<sub>2</sub>T contains

a high CNT content, this graphite-related oxidation peak is more pronounced. During the reduction process, the peak at 0.21 V corresponds to lithium insertion into the silicon anode.<sup>[28]</sup> In the first three cycles, the increasing current intensity of the reduction peak suggests that the activity of the silicon anode gradually improves during the initial charge/discharge cycles. The pseudocapacitive behavior of the materials is analyzed through CV at different scan rates of 0.1, 0.2, 0.5, and 1.0 mVs<sup>-1</sup> (Figure S6, Supporting Information). Based on the fitted slope values (b-values) derived from the log(i)-log(v) relationship,<sup>[29,30]</sup> the b-values for SiVG and SiVG<sub>2</sub>T were 0.975 and 0.997; 0.947 and 0.962, respectively (Figure S7, Supporting Information). These results indicate that the silicon-carbon composite materials exhibit both battery-type (diffusion-controlled) and pseudocapacitive (capacitive-controlled) behaviors.<sup>[31]</sup> SiVG<sub>2</sub>T shows a lower b-value, suggesting that it exhibits a stronger battery-type behavior and the weakest pseudocapacitive contribution. In this context, battery-type behavior corresponds to diffusion-controlled kinetics, while pseudocapacitive behavior is governed by surface capacitance. For LIB anode materials, a lower b-value within a certain range indicates better control by diffusion processes and a reduced pseudocapacitive effect, which is desirable for long-term cycling and high energy density, as illustrated in (Figure S5, S6, Supporting Information). The pseudocapacitive contribution can be estimated by integration. With the capacitive region of SiVG and SiVG<sub>2</sub>T being 80.3% and 79.3% respectively, the battery-type behaviors of both are governed by capacitive control at 0.5 mV s<sup>-1</sup>, as shown in (Figure S8, S9, Supporting Information). The percentage of pseudocapacitive contributions of SiVG and SiVG<sub>2</sub>T are 74.6%–96.1% and 67.4%–90.7%, respectively, from 0.1 to 1.0 mVs<sup>-1</sup> (Figure S10, Supporting Information). In the galvanostatic intermittent titration technique (GITT) test, a titration current of 0.1 Ag<sup>-1</sup> was applied. The full discharge time for SiVG was 108 h, while that for SiVG<sub>2</sub>T was 79.5 h. The discharge duration is positively correlated with the silicon

content, indicating that the GITT profiles reflect the compositional ratios of the materials. Furthermore, the lithium-ion diffusion coefficients for SiVG and SiVG<sub>2</sub>T ranged from  $9.57 \times 10^{-9}$  to  $6.26 \times 10^{-14} \text{ cm}^2 \text{ s}^{-1}$  and from  $1.45 \times 10^{-8}$  to  $9.36 \times 10^{-14} \text{ cm}^2 \text{ s}^{-1}$ , respectively. The increase in diffusion coefficient with CNTs addition suggests that lithium-ion transport is enhanced, likely due to improved electronic conductivity and high structural stability of conductive network of electrodes from the CNTs network, which facilitates better charge transport. These results are shown in Figure 4g,h. In LIB anodes, the impedance before cycling typically ranges in the tens of ohms, but it decreases to below 10 Ω after cycling. The low-frequency slope of the EIS curve (Figure S12, Supporting Information), specifically, the slope after the second intersection with the x-axis, reflects the ion transport capability,<sup>[32]</sup> a larger slope indicates better ion transport performance. SiVG demonstrates poor ion transport, primarily because in the absence of CNT coating, the ion migration is affected by slow electron transport, resulting in slower ion movement. However, SiVG<sub>2</sub>T exhibits a steeper slope in the impedance curve, indicating enhanced ion transport capability.<sup>[33]</sup> This is likely due to the positive role of CNTs, which act as electron-conducting materials and promote lithium-ion transport to some extent.<sup>[34]</sup> The long cycling stability is tested under 5 Ag<sup>-1</sup> for 1000 cycles, after which the capacities of 344.1 and 699.7 mAh g<sup>-1</sup> are obtained for SiVG and SiVG<sub>2</sub>T, with the corresponding capacity retentions of 48.8% and 78.0%, respectively. The SiVG<sub>2</sub>T provides sufficient space for silicon to expand during the cycling, maintaining the active materials high stability. The obtained rate performances and cycling stability of SiVG<sub>2</sub>T are superior to almost all of the reports on the silicon-carbon anodes in LIBs.

During the cycling of silicon-carbon anodes, the substantial volume expansion of silicon often leads to significant internal stress variations within the anode, resulting in issues such as pulverization and cracking of active materials. In the case of SiVG, large surface cracks are observed after 100 cycles, as shown in

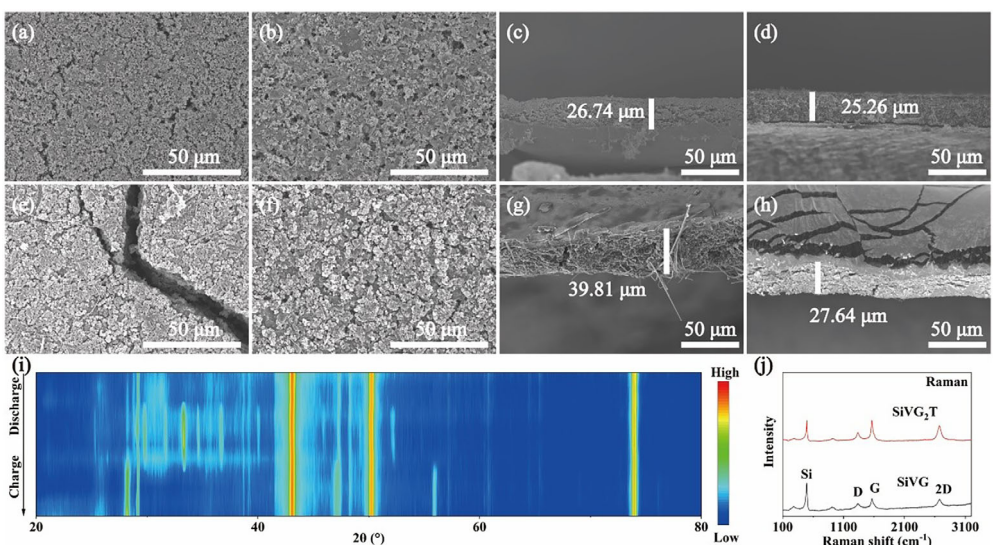


**Figure 5.** Before cycling a) the electrode surface of SiVG, b) the electrode surface of SiVG<sub>2</sub>T, c) the cross-section of SiVG electrode, d) the cross-section of SiVG<sub>2</sub>T anode. After cycling e) the electrode surface of SiVG, f) the electrode surface of SiVG<sub>2</sub>T, g) the cross-section of SiVG electrode, h) the cross-section of SiVG<sub>2</sub>T electrode. i) Ex situ XRD pattern of SiVG<sub>2</sub>T. j) Raman spectra of SiVG and SiVG<sub>2</sub>T after cycling.

**Figure 5a,e.** In contrast, SiVG<sub>2</sub>T demonstrates much better performance, with the electrode surfaces remaining relatively smooth and uniform before and after cycling, as seen in Figure 5b,f. While surface SEM images reflect interfacial stability, cross-sectional images provide insights into internal structural changes caused by stress. The thickness changes of SiVG and SiVG<sub>2</sub>T electrodes are  $\approx$ 49.0% (Figure 5c,g) and 2.6% (Figure 5d,h), respectively. Although the VG in SiVG provides strain-reserving voids, the stacking of VG on the microspheres occupies these voids that relate to smaller porosity, resulting in significant expansion after cycling. SiVG<sub>2</sub>T, with its outer CNT coating, better utilizes the reserved strain space, effectively minimizing volume expansion by proper porosity. Therefore, the 3D stress-buffering network constructed by CNTs and VG efficiently alleviates the volume expansion issues of silicon during cycling, thus obtaining a stable silicon-carbon anode with higher cycling stability. In ex situ XRD analysis (Figure 5i), three red peaks are typically attributed to

the copper foil current collector substrate. During discharge, structural changes are observed in the diffraction angle range of 30°–40°, indicating progressive alloying between lithium and silicon. As the content of Li–Si alloy increases, new crystalline phases of Li–Si alloys appear, with characteristic peaks corresponding to the (332), (431), and (220) planes at  $\approx$ 42°, 46°, and 52°, respectively.<sup>[35]</sup> During charging, the crystalline silicon peaks at (111), (220), and (311), located at 28.4°, 47.3°, and 56.1°, respectively, gradually reappear, although the peaks are broader and less intense than before cycling, indicating lower crystallinity. After the charging plateau, the Li–Si alloy peaks gradually disappear. The ex situ XRD patterns clearly depict the transformation of silicon from crystalline silicon to alloyed silicon and back to silicon during the charge/discharge process. After undergoing the same number of charge/discharge cycles, the structural and compositional changes in the SiVG and SiVG<sub>2</sub>T anodes are analyzed using XRD and Raman spectroscopy. After disassembly and charging at a

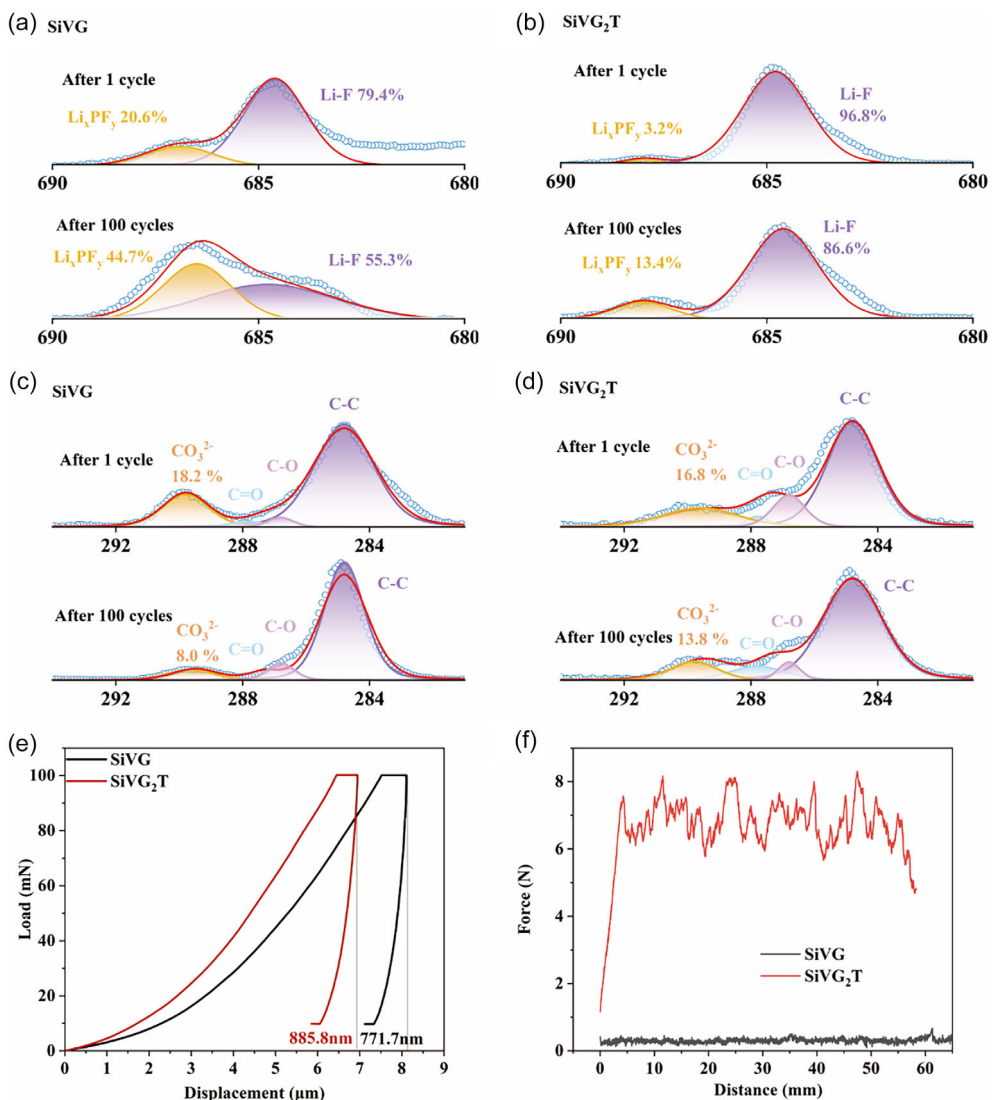


**Figure 6.** SEI composition analysis by XPS at different cycle numbers: a,b) F 1s spectra of SiVG (a) and SiVG<sub>2</sub>T (b) electrodes, c,d) C1s spectra of SiVG (c) and SiVG<sub>2</sub>T (d) electrodes. e) Nanoindentation curves of SiVG and SiVG<sub>2</sub>T electrodes. f) Peel strength curves of SiVG and SiVG<sub>2</sub>T electrodes.

current density of  $1 \text{ A g}^{-1}$ , the electrodes are examined. Due to the relatively high current, complete delithiation is not achieved. The XRD results reveal distinct diffraction peaks corresponding to the (111), (220), and (311) planes of crystalline silicon at  $28.4^\circ$ ,  $47.3^\circ$ , and  $56.1^\circ$ , respectively, along with several peaks attributable to residual Li–Si alloy phases, indicating incomplete delithiation (see Figure S11, Supporting Information). Raman spectra (Figure 5j) further reveal that the silicon characteristic peaks become broader after cycling, indicating a reduction in crystallinity. This suggests that the repeated cycling makes silicon partially amorphous. In the case of SiVG<sub>2</sub>T, the silicon is almost entirely encapsulated within the 3D carbon network formed by CNTs and VG. This encapsulation is reflected in the stronger relative carbon peaks in the Raman spectra, suggesting effective protection and improved cycling stability. Moreover, the enhanced carbon-related peaks in the postcycling Raman spectra confirm the structural integrity of the CNT framework on the electrode surface, indicating that the 3D carbon network remains intact and functions effectively throughout the cycling process.

To investigate the correlation between the SEI composition and the electrode thickness evolution during cycling, XPS analyses of F and C elements were performed on the electrode surfaces after the first and 100th cycles. Compared with SiVG (Figure 6a), the SEI of the SiVG<sub>2</sub>T electrode contains a higher amount of LiF and exhibits a smaller variation in LiF content with increasing cycle number (Figure 6b). A LiF-rich SEI is beneficial for ion transport and enhances the mechanical robustness of the SEI, thereby improving rate performance and cycling stability.<sup>[36]</sup> Similarly, the C 1s spectra of SiVG (Figure 6c) show more pronounced compositional changes upon cycling than those of SiVG<sub>2</sub>T (Figure 6d). The extent of SEI compositional variation is closely related to electrode volume expansion: larger expansion leads to repeated fracture and regeneration of the SEI, resulting in compositional instability, the formation of more organic species, and a reduction in inorganic components. As shown in Figure 5, compared with SiVG<sub>2</sub>T, the SiVG electrode exhibits a larger change in electrode thickness after 100 cycles, leading to a less stable SEI. The mechanical performance of electrodes after 100 cycles is measured by the nanoindentation tests. Applied to the same load, the curve slope of the SiVG<sub>2</sub>T electrode is steeper than that of SiVG in the loading stage, indicating that SiVG<sub>2</sub>T has a higher modulus to resist outer pressure.<sup>[37]</sup> After unloading, the larger displacement recovery of SiVG<sub>2</sub>T suggests better elastic recovery (Figure 6e). Figure 6f illustrates the peel strength of the electrodes after 100 cycles, in which SiVG<sub>2</sub>T exhibits higher peel strength than SiVG due to its lower electrode thickness expansion (Figure 5) to enhance the interaction between active materials and current collector.<sup>[38]</sup> The above results further confirm the excellent structural stability of SiVG<sub>2</sub>T electrodes after long cycles.

### 3. Conclusions

In conclusion, a novel SiVG<sub>2</sub>T stable anode material is prepared by spray drying, in this research, which encapsulates silicon nanoparticles in vertically aligned graphene with CNTs. CNTs driven by

surface tension as the solvent vaporizes cover the top of VGs to form the network structure. The 3D interconnected robust carbon network in which VGs and CNTs are perpendicular in microspheres provides efficient strain-reserving voids to reduce volumetric expansion of Si during cycling, enhancing electron and lithium-ion transportation effectively. The lithium ions are transported rapidly along VGs, cooperating with the electrons conducted by CNTs from the collectors. Consequently, the ion and electron transport enhance each other. With these features, SiVG<sub>2</sub>T exhibits sufficient capacity of lithium-ion storage, low expansion rate, distinguished rate capability, and excellent interfacial stability. After cycling, the anode with SiVG<sub>2</sub>T gains 2.6% expansion in the cross-section direction, endowing it with reliable cycling stability for potentially commercial use. The rate capability reaches  $904 \text{ mAhg}^{-1}$  at  $5 \text{ Ag}^{-1}$  with a high capacity retention of 78.0% after 1000 cycles and  $418 \text{ mAhg}^{-1}$  at  $20 \text{ Ag}^{-1}$ , and only displays a thickness change of 2.6% in the cross-section direction after 100 cycles at  $0.5 \text{ Ag}^{-1}$ . This work provides an innovative view of the CNT and vertical graphene cooperative effect in porous silicon–carbon anode materials for advanced commercial LIBs, and also provides an analysis of the lithium-ion storage mechanism.

### Acknowledgements

This work was financially supported by Guangdong Major Project of Basic and Applied Basic Research (2023B030300002), Shenzhen Key Laboratory of Advanced Energy Storage (ZDSYS202204011 41000001), and High level of special funds (G03034K001). The authors would also like to acknowledge the technical support from SUSTech Core Research Facilities and thank Xueyanhui (<https://www.xueyanhui.com>) for plotting the diagrams.

### Conflict of Interest

The authors declare no conflict of interest.

### Author Contributions

**Fenghua Yu and Yongbiao Mu:** conceived the idea, designed the experiments, conducted the characterizations, and co-wrote the paper, **Kunxiong Zheng, Hengyuan Hu, Zhiyu Zou, and Yuankai Huang:** assisted with material synthesis and conducted the characterizations, **Wenjia Li:** revised the manuscript and triggered helpful discussion, **Tianshou Zhao, Meisheng Han, Lin Zeng, and Lei Wei:** supervised the project and co-revised the paper. All the authors discussed the results and provided comments and revisions to the manuscript. **Fenghua Yu and Yongbiao Mu** contributed equally to this work.

### Data Availability Statement

The data that support the findings of this study are available from the corresponding author upon reasonable request.

**Keywords:** carbon nanotube network • lithium-ion batteries • silicon–carbon composite anode • vertically aligned graphene • volumetric expansion mitigation

- [1] B. Dunn, H. Kamath, J.-M. Tarascon, *Science* **2011**, *334*, 928.
- [2] Y. Mu, H. Hu, Z. Li, Y. Chu, Z. Zou, Y. Chen, J. Guan, M. Han, Q. Zhang, L. Zeng, *Renewables* **2025**, *3*, 135.
- [3] Y. Fu, D. Li, X. Sun, Y. Xue, Y. Shi, Z. Li, C. Luo, Q. Lin, X. Gui, K. Xu, *Small* **2024**, *20*, 2403070.
- [4] F. Duffner, N. Kronemeyer, J. Tübke, J. Leker, M. Winter, R. Schmuck, *Nat. Energy* **2021**, *6*, 123.
- [5] H. Zhang, R. Hu, S. Feng, Z. Lin, M. Zhu, *eScience* **2023**, *3*, 100080.
- [6] J. D. McBrayer, M.-T. F. Rodrigues, M. C. Schulze, D. P. Abraham, C. A. Apblett, I. Bloom, G. M. Carroll, A. M. Colclasure, C. Fang, K. L. Harrison, G. Liu, S. D. Minteer, N. R. Neale, G. M. Veith, C. S. Johnson, J. T. Vaughney, A. K. Burrell, B. Cunningham, *Nat. Energy* **2021**, *6*, 866.
- [7] P. Zhou, P. Xiao, L. Pang, Z. Jiang, M. Hao, Y. Li, F. Wu, *Adv. Funct. Mater.* **2025**, *35*, 2406579.
- [8] M. Han, Y. Mu, J. Guo, L. Wei, L. Zeng, T. Zhao, *Nano-Micro Lett.* **2023**, *15*, 80.
- [9] Z. Li, M. Han, P. Yu, J. Lin, J. Yu, *Nano-Micro Lett.* **2024**, *16*, 98.
- [10] D. Wang, C. Zhou, B. Cao, Y. Xu, D. Zhang, A. Li, J. Zhou, Z. Ma, X. Chen, H. Song, *Energy Storage Mater.* **2020**, *24*, 312.
- [11] X. Guan, Y. Zhang, I. A. Kinloch, M. A. Bissett, *ACS Appl. Mater. Interfaces* **2025**, *17*, 10580.
- [12] X. Lin, J. Li, L. Dai, K. Pei, Z. Huang, S. Huang, M. Li, Y. Liang, H. Chen, S. Zhang, *Nano Energy* **2025**, *139*, 110957.
- [13] H. Liu, Q. Sun, H. Zhang, J. Cheng, Y. Li, Z. Zeng, S. Zhang, X. Xu, F. Ji, D. Li, J. Lu, L. Ci, *Energy Storage Mater.* **2023**, *55*, 244.
- [14] J. Shen, S. Zhang, H. Wang, R. Wang, Y. Hu, Y. Mao, R. Wang, H. Zhang, Y. Du, Y. Fan, Y. Zhou, Z. Guo, B. Wang, *eScience* **2024**, *4*, 100207.
- [15] M. Han, Y. Mu, L. Wei, L. Zeng, T. Zhao, *Carbon Energy* **2024**, *6*, e377.
- [16] Z. Li, M. Han, J. Yu, *Rare Met.* **2023**, *42*, 3692.
- [17] Y. Mu, Y. Chen, B. Wu, Q. Zhang, M. Lin, L. Zeng, *Adv. Sci.* **2022**, *9*, 2203321.
- [18] L. Wang, Y. Zhao, H. Zhang, H. Wang, C. Chen, Y. Huang, H. Xue, Y. Lan, F. Qiao, J. Wang, Z. Lou, F. Pan, *Energy Storage Mater.* **2025**, *78*, 104255.
- [19] X. Wang, Q. Hu, J. Cui, J. Hou, Y. Huang, X. Liu, *ACS Appl. Mater. Interfaces* **2025**, *17*, 12004.
- [20] M. Han, Y. Mu, F. Yuan, J. Liang, T. Jiang, X. Bai, J. Yu, *J. Mater. Chem. A* **2020**, *8*, 3822.
- [21] S. Wu, H. Wu, X. Kong, Y. Li, G. Xu, J. Su, J. Huang, G. Wang, X. Ou, *Chem. Eng. J.* **2024**, *502*, 158032.
- [22] Z. He, Z. Xiao, H. Yue, Y. Jiang, M. Zhao, Y. Zhu, C. Yu, Z. Zhu, F. Lu, H. Jiang, C. Zhang, F. Wei, *Adv. Funct. Mater.* **2023**, *33*, 2300094.
- [23] Z. He, C. Zhang, Y. Zhu, F. Wei, *Energy Environ. Sci.* **2024**, *17*, 3358.
- [24] P. Huang, Z. Guo, Z. Li, L. Chen, W. D. Liu, J. Luo, Z. Liu, J. Zhang, J. Zeng, W. Zhang, X. Zhang, R. Zhu, Y. Chen, *Adv. Mater.* **2025**, *37*, 2507521.
- [25] R. Liu, C. Shen, Y. Dong, J. Qin, Q. Wang, J. Iocozzia, S. Zhao, K. Yuan, C. Han, B. Li, Z. Lin, *J. Mater. Chem. A* **2018**, *6*, 14797.
- [26] X. Zou, M. Li, H. Li, G. Cao, Q. Jiang, R. Duan, H. Qian, J. Li, X. Yang, Y. Cao, J. Wang, H. Li, Y. Ma, X. Li, *Chem. Eng. J.* **2024**, *498*, 155573.
- [27] P. Yu, Z. Li, M. Han, J. Yu, *Small* **2024**, *20*, 2307494.
- [28] H. Li, B. Yao, M. Li, X. Zou, R. Duan, H. Li, Q. Jiang, G. Cao, J. Li, H. Yan, N. Xu, B. Sun, J. Wang, X. Li, *ACS Appl. Mater. Interfaces* **2024**, *16*, 53665.
- [29] Z. Yi, N. Lin, W. Zhang, W. Wang, Y. Zhu, Y. Qian, *Nanoscale* **2018**, *10*, 13236.
- [30] R. Zhao, H. Di, C. Wang, X. Hui, D. Zhao, R. Wang, L. Zhang, L. Yin, *ACS Nano* **2020**, *14*, 13938.
- [31] Z. Liu, D. Lu, W. Wang, L. Yue, J. Zhu, L. Zhao, H. Zheng, J. Wang, Y. Li, *ACS Nano* **2022**, *16*, 4642.
- [32] H. J. Kwon, J. Y. Hwang, H. J. Shin, M. G. Jeong, K. Y. Chung, Y. K. Sun, H. G. Jung, *Nano Lett.* **2020**, *20*, 625.
- [33] R. Shao, J. Niu, F. Zhu, M. Dou, Z. Zhang, F. Wang, *Nano Energy* **2019**, *63*, 103824.
- [34] T. Mu, S. Lou, N. G. Holmes, C. Wang, M. He, B. Shen, X. Lin, P. Zuo, Y. Ma, R. Li, C. Du, J. Wang, G. Yin, X. Sun, *ACS Appl. Mater. Interfaces* **2021**, *13*, 4093.
- [35] J. Li, J. R. Dahn, *J. Electrochem. Soc.* **2007**, *154*, A156.
- [36] M. Han, J. Liu, K. Zheng, C. Deng, Y. Mu, J. Guo, Y. Chu, Z. Zou, F. Yu, W. Li, L. Wei, L. Zeng, T. Zhao, *Adv. Energy Mater.* **2024**, *14*, 2401065.
- [37] Y. Mu, Y. Chu, Y. Shi, C. Huang, L. Yang, Q. Zhang, C. Li, Y. Feng, Y. Zhou, M. Han, T. Zhao, L. Zeng, *Adv. Energy Mater.* **2024**, *14*, 2400725.
- [38] A. M. Gaikwad, A. C. Arias, *ACS Appl. Mater. Interfaces* **2017**, *9*, 6390.

Manuscript received: August 22, 2025

Revised manuscript received: October 13, 2025

Version of record online: